Pressure- and stress-induced fabric transition in olivine from peridotites in the Western Gneiss Region (Norway): implications for mantle seismic anisotropy

Q. WANG, Q-K. XIA, S. Y. O'REILLY, W. L. GRIFFIN, E. E. BEYER AND H. K. BRUECKNER

Appendix S1: Analytical methods

1. Major-element composition of whole-rock samples

The major-element compositions of whole-rock samples were analyzed by X-ray fluorescence (XRF) using methods described by O'Reilly & Griffin (1988). Except for samples K-i-I and I-A, which were measured in the State Key Laboratory for Mineral Deposits Research, Nanjing University, all other analyses were carried out in the Geochemical Analysis Unit (GAU) at the ARC National Key Centre GEMOC National Key Centre in the Department of Earth and Planetary Sciences, Macquarie University. The data for peridotites from Almklovdalen were published by Beyer *et al.* (2006). The results are shown in Table S1 & Fig. 3.

2. Major-element composition of olivine, orthopyroxene and clinopyroxene

The major-element compositions of minerals for the three Tafjord dunite samples TO, K-i-I and I-A were determined using a JEOL Superprobe (JXA 8100) electron microprobe analyzer at Nanjing University, China. Analyses were performed with 15 kV accelerating voltage, 10 nA beam current and <5 mm beam diameter. Natural minerals and synthetic oxides were used as standards, and a program based on the ZAF procedure was used for data correction. Twelve to 15 olivine grains were measured in each sample.

All the other analyses were performed on a CAMEBAX SX50 at Macquarie University. A range of natural standards was used, together with standard matrix correction procedures. Count times used were 10 s for peaks with 5 s for backgrounds on either side of the peak. The major-element composition of olivine, orthopyroxene and clinopyroxene are given in Tables S2, S3 and S4, respectively.

3. Microstructure analysis

Except for the three Tafjord dunite samples TO, K-i-I and I-A, the crystallographic preferred orientations (CPOs) of olivine, orthopyroxene and clinopyroxene were measured using a scanning electron microscope JEOL JSM-5610LV by electron backscatter diffraction (EBSD) technique and the HKL Channel 5+ software in the State Key Laboratory for Continental Tectonics and Dynamics, Institute of Geology in Beijing, China. Carefully polished thin sections were put in the microscope chamber with 70° tilt angle. The electron backscatter patterns were acquired at accelerating voltage of 20 kV and a working distance of 20 mm. The whole surface of each sample was analyzed in an automatic procedure with a step size of 50 μm for samples N97-5, N97-14, N97-18, N97-8, N97-9, N97-13, GBWG and N97-30, and 30 μm for samples N97-40 and N97-41. The subsets of one point per grain, coarse grains (>300 μm), and small grains (<150 μm) are obtained by using HKL Channel 5+ software. Then the pole figures of olivine were plotted for the complete dataset and each subset.

For serpentinized garnet harzburgites N97-40 and N97-41, because the grain size of olivine and enstatite is generally > 100 μm, a step size of 30 μm is enough to cover small grains. For other samples with porphyroclastic texture, the step size of 50 μm in the EBSD analysis may not be able to distinguish the fabrics of small new grains. In order to compare the fabrics of recrystallized new grains and porphyroclasts, the

EBSD mapping was undertaken with a step size of 10 μm on areas dominated by recrystallized grains. The analysis was carried out in a scanning electron microscope JEOL JSM-6490 in the State Key Laboratory for Mineral Deposits Research at Nanjing University, China. The accelerating voltage is 20 kV and a working distance is 20 mm. The pole figures of locally recrystallized olivine are shown in Fig. S1. For the samples with porphyroclastic texture (N97-5, N97-14, N97-18, GBWG & N97-30) and shape preferred orientation (samples N97-8, N97-9 & N97-13), the CPOs derived from 10 μm are consistent with those using the subsets of small grains from complete data.

The CPO of olivine for samples TO, K-i-I and I-A was studied in a FEI Quanta 450 FEG with an accelerating voltage of 20 kV and a working distance of 25 mm in the State Key Laboratory for Geological Processes and Mineral Resources at University of Geosciences, Wuhan, China. Because the grain size of the three samples is dominated by ~0.5 mm, the step size was set as 200 μm for samples TO and I-A, and 250 μm for sample K-i-I. The subsets of one point per grain and small grains (<250 μm) are obtained by using HKL Channel 5+ software. Manual indexing omitted the large porphyroclasts. The olivine fabrics using the complete dataset, subsets of one point per grain and small grains, and manually indexed points are given in Table 2.

Pole figures of indexed phases and seismic properties of peridotite were calculated using the CAREWARE petrophysics software of Mainprice (1990). To eliminate poorly indexed points, the accepted maximum value of mean angular deviation was set at 1.2. The pole figures of olivine, orthopyroxene, and clinopyroxene using complete dataset are shown in Figs 5-6, Figs S4-S5 & Fig. S6, respectively.

4. Water content measurements

Water contents of olivine were measured using the Fourier transform infrared (FTIR) analysis on a Nicolet 5700 FTIR spectrometer coupled with a Continuum microscope at the University of Science and Technology of China (USTC). Unpolarized spectra were obtained from 1000 to 5000 cm^{-1}, using a KBr beam splitter and a liquid-nitrogen cooled MCT-A detector. A total of 128 or 256 scans were accumulated for each spectrum at a 4 cm^{-1} resolution. The aperture size was set to 100 × 100 μm for coarse grains, and 25 × 25 μm for small grains. Measurements were made through optically clean, inclusion- and crack-free areas (usually the core region of selected grains) under a continuous dry N_2 gas flush.

A modified form of the Beer-Lambert law was used to calculate the H_2O contents:

$$c=A/(I\times t)$$

where c is the content of hydrogen species (ppm H_2O wt %), A is the integrated area (cm^{-2}) of absorption bands in the region of interest, I is the integral specific absorption coefficient (ppm^{-1} cm^{-2}), and t is thickness (cm). OH absorption bands were integrated between 3000 and 3800 cm^{-1} and multiplied by 3 to obtain A values (Kovacs *et al.*, 2008). The integral specific coefficients of 0.188 ppm^{-1} cm^{-2} was used (Bell *et al.*, 2003) to calculate H_2O contents. Thickness was measured using a digital micrometer and is reported as the average of 30-40 measurements covering the whole section.

Baseline corrections were carried out by hand, at least three times for each spectrum, the uncertainty was < 5%, and the average corrected spectrum was used to calculate H_2O contents.

To minimize possible uncertainties from the unpolarized radiation, 15–30 grains were analysed in each section, and the average H_2O content of olivine calculated for that sample. Uncertainties in the calculated H_2O contents come from (1) using unpolarized infrared beams on unoriented minerals (<10%, Kovacs *et al*., 2008); (2) baseline correction (<5%); (3) variable sample thickness (<3%); and (4) differences between the absorption coefficients (<10%) of our samples and those of samples used by Bell *et al.* (2003) due to differences in composition. The total uncertainty is estimated to be < 30%. Our results are ~3.5 times the values derived from the Paterson (1982) calibration (Bell *et al*., 2003).

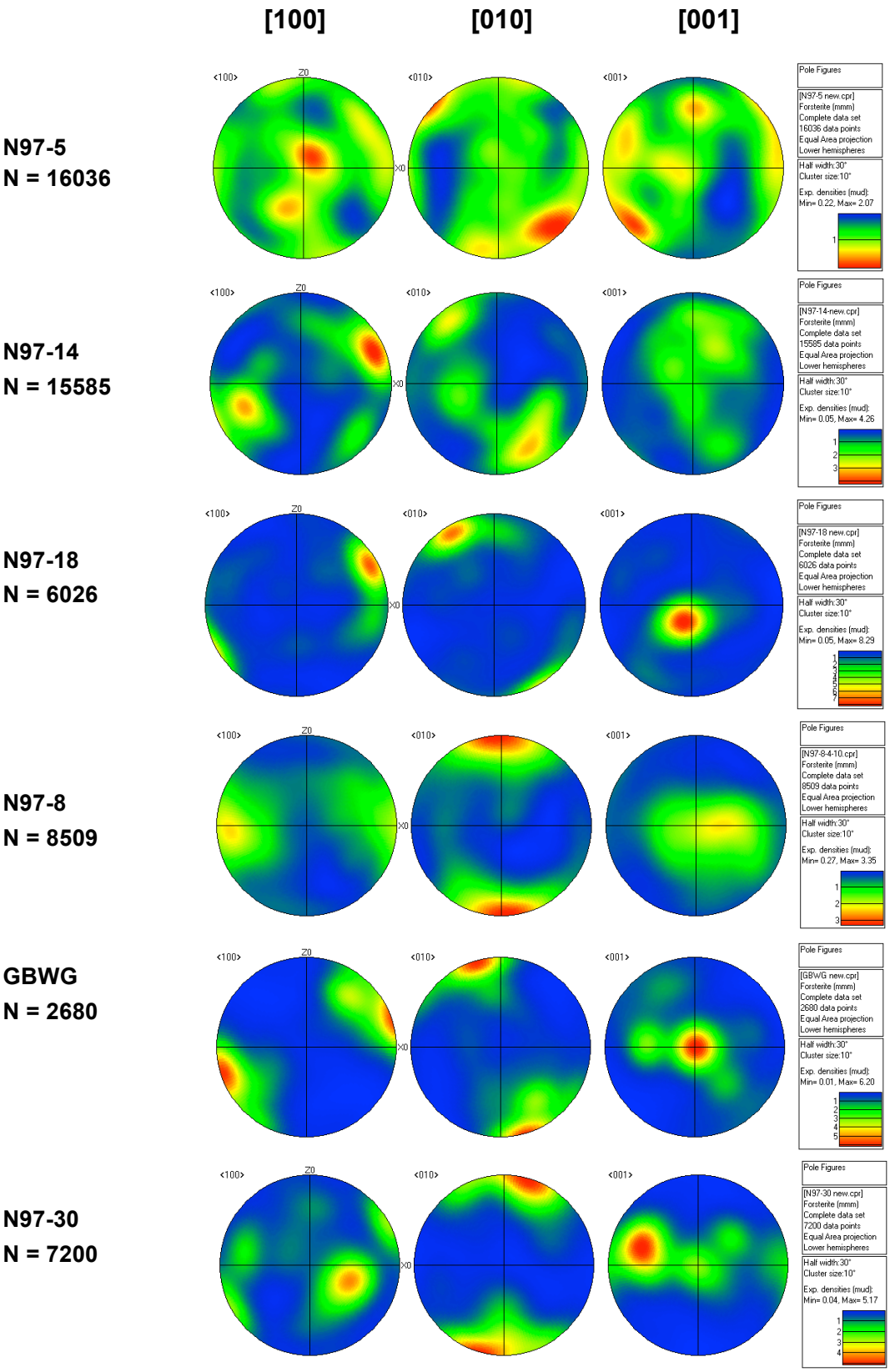

Figure S1. Equal-area lower hemisphere projection of olivine crystal axis distribution for recrystallized small grains using a step size of 10 μm in the EBSD analysis. N is number of data points. X0 is parallel to the lineation and Z0 is normal to the foliation.

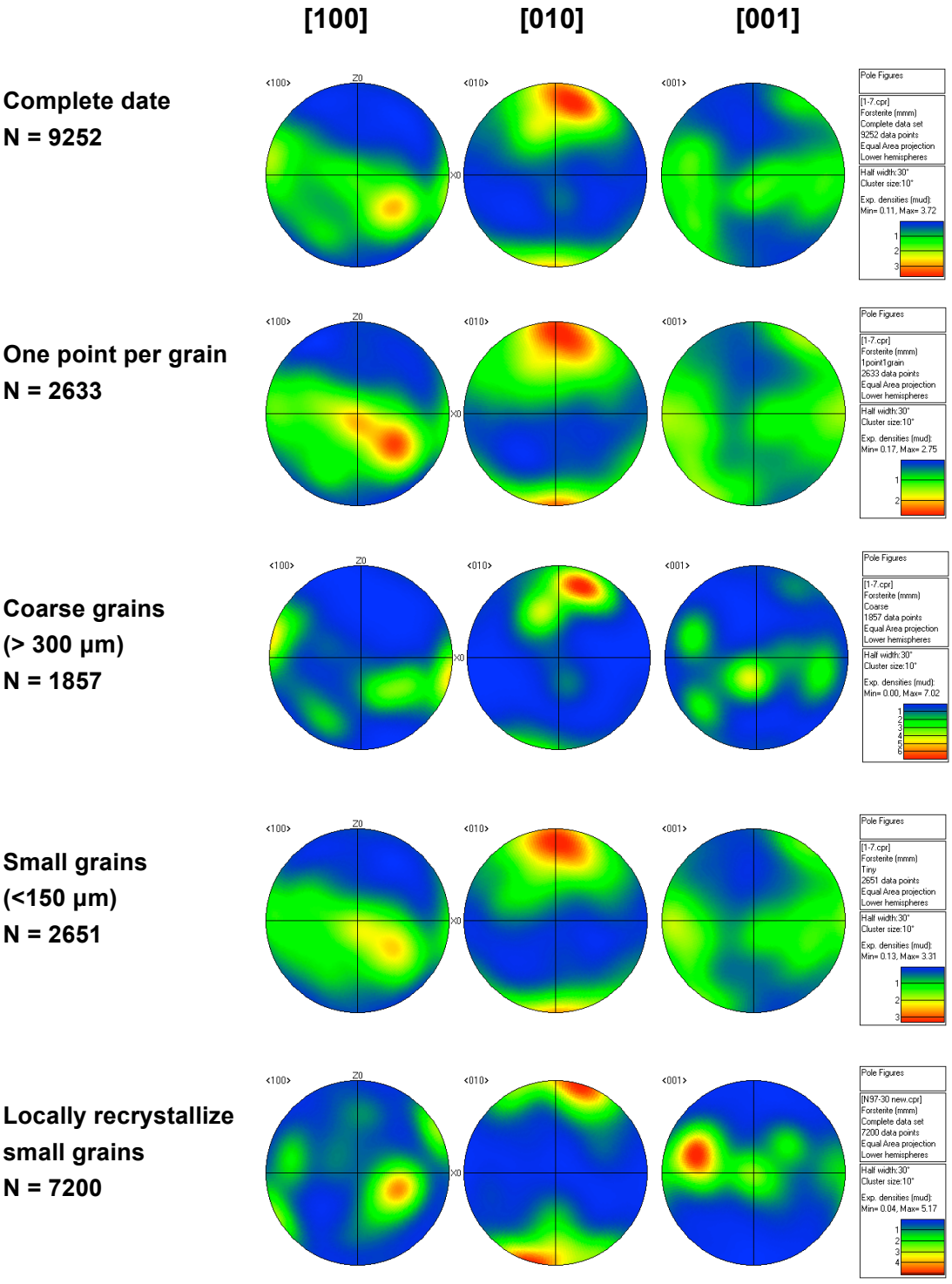

Figure S2. Equal-area lower hemisphere projection of olivine crystal axis distribution for sample N97-30. The pole figures of olivine show [001](010) fabric for complete data, subsets of one point per grain, small grains and locally recrystallized small grains, but [100](010) fabric for a subset of coarse grain. N is number of data points. X0 is parallel to the lineation and Z0 is normal to the foliation.

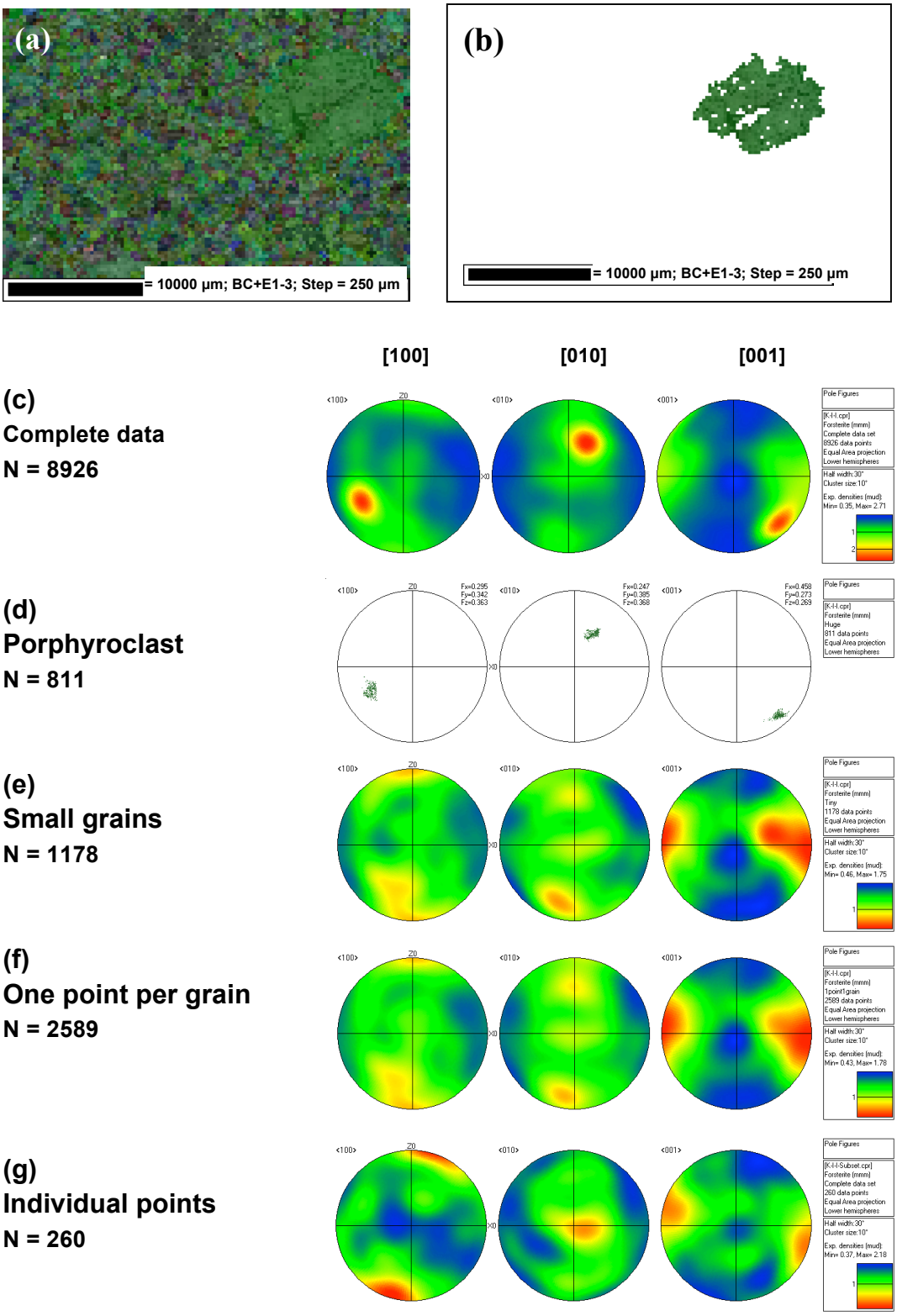

Figure S3. EBSD map with band contrast and all Euler angles for (a) a strongly sheared, porphyroclastic dunite K-i-I, and (b) a large olivine porphyroclast in the thin section, and pole figures of olivine using (c) complete data set, subsets of (d) the large olivine porphyroclast, (e) small grains (<300 µm), (f) one point per grain, and (g) manually indexed individual olivine points. N is number of data points. X0 is parallel to the lineation and Z0 is normal to the foliation.

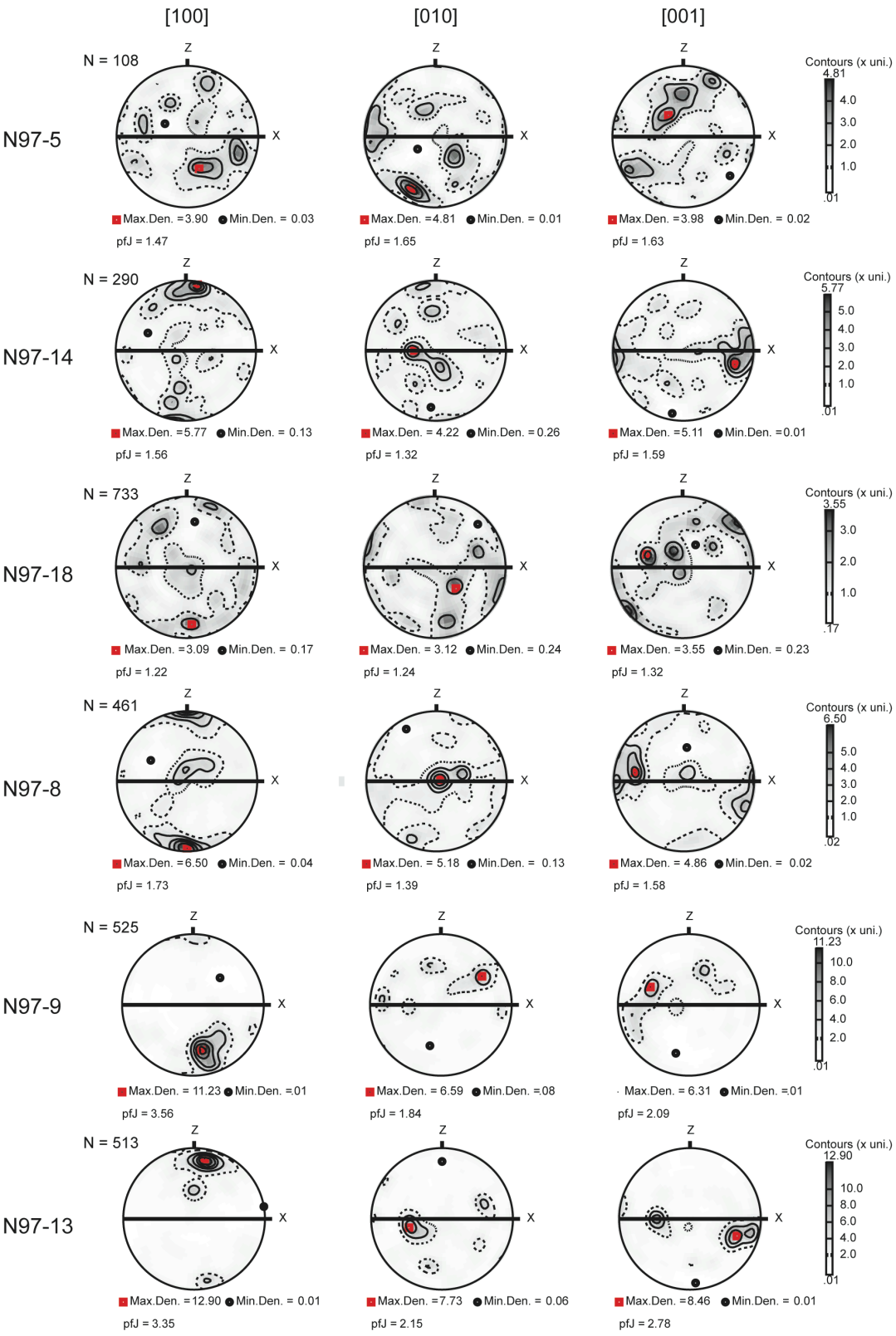

Figure S4. Equal-area lower hemisphere projection of enstatite crystal axis distribution for the Almklovalen peridotites. N: number of data points; pfJ: texture index. X is parallel to the lineation and Z is normal to the foliation. The contours at multiples of a uniform distribution are plotted in an inverse log grey scale to emphasize high densities.

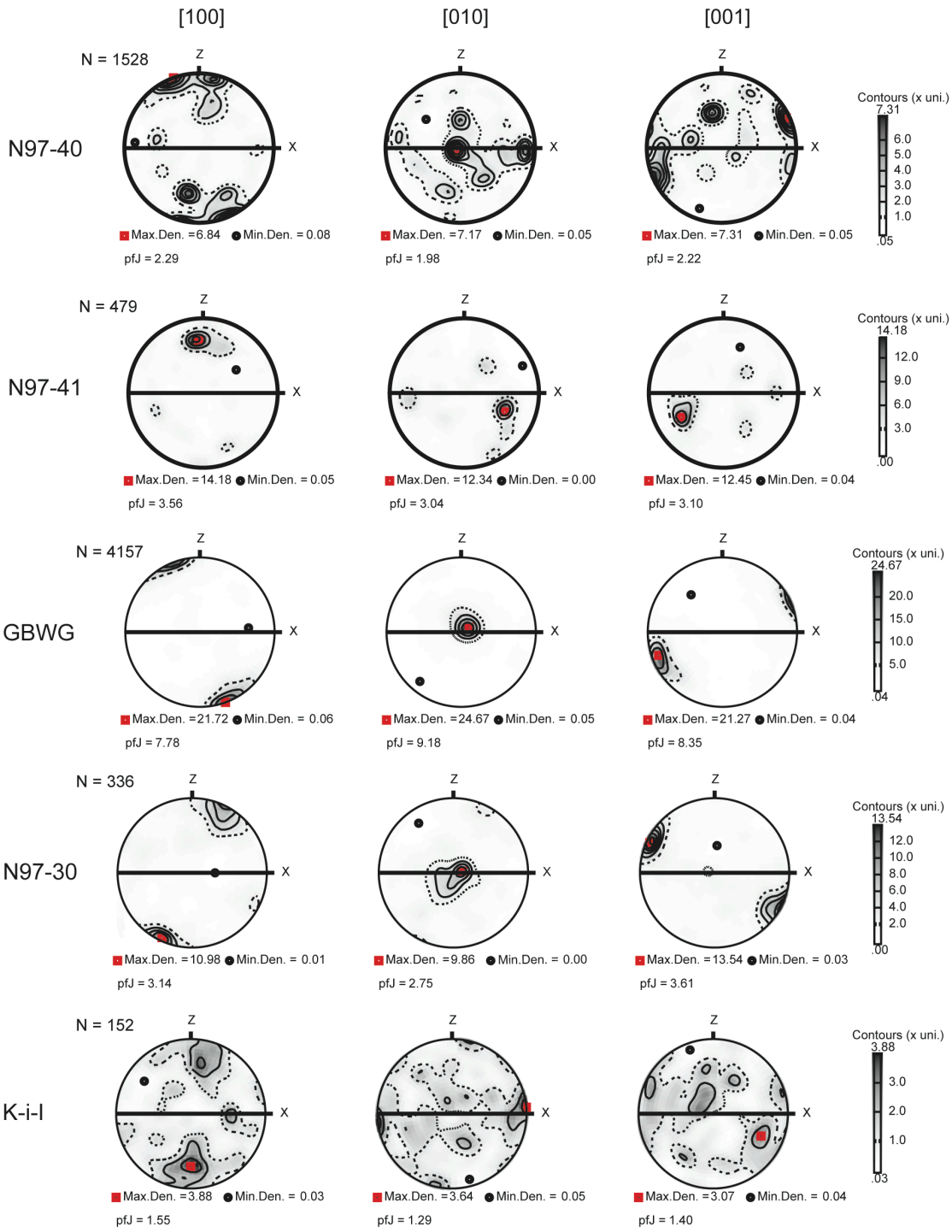

Figure S5. Equal-area lower hemisphere projection of enstatite crystal axis distribution for peridotites from Ugelvik, Gurskebotn and Kallskaret. N: number of data points; pfJ: texture index. X is parallel to the lineation and Z is normal to the foliation. The contours at multiples of a uniform distribution are plotted in an inverse log grey scale to emphasize high densities.

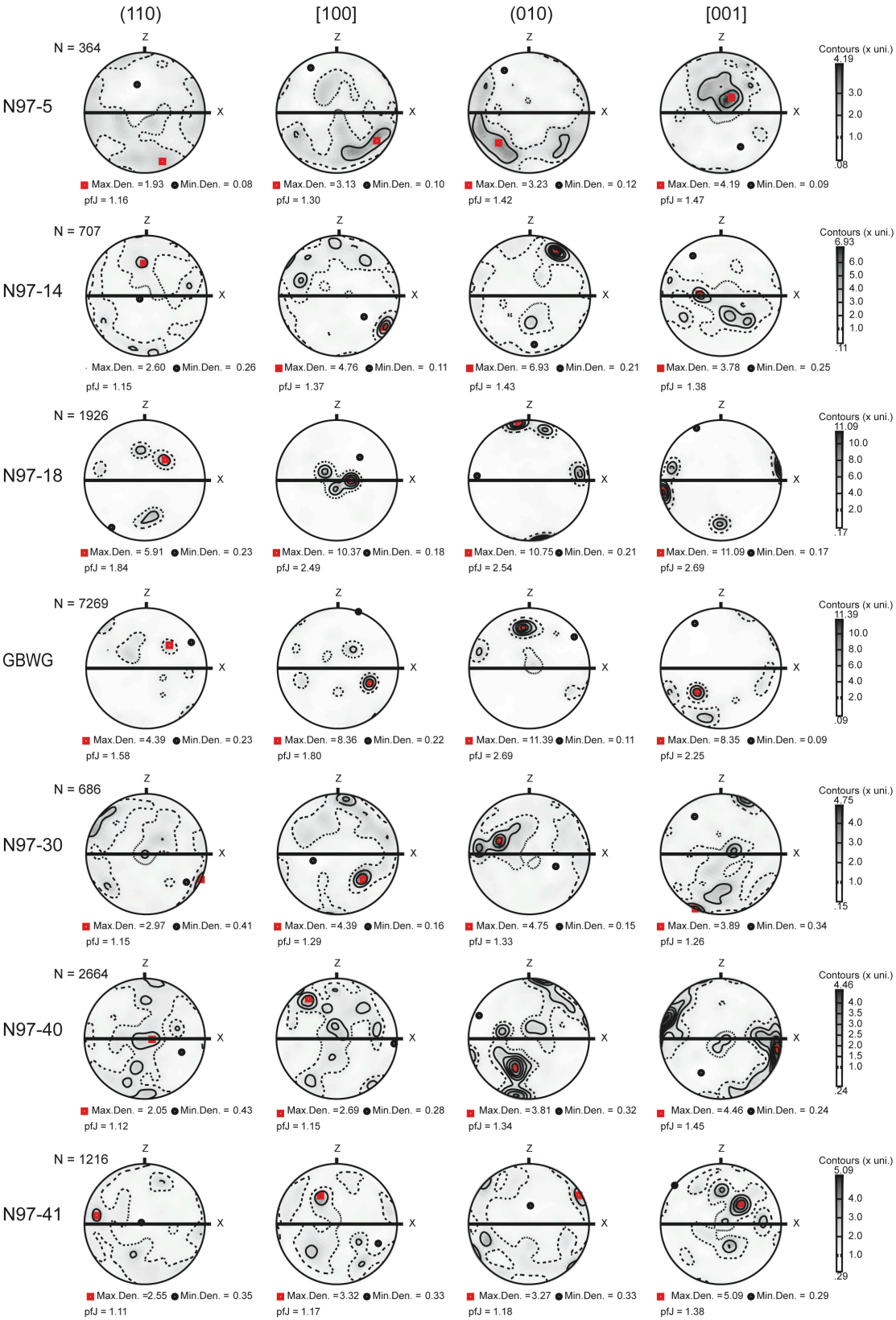

Figure S6. Equal-area lower hemisphere projection of diopside crystal axis distribution for the WGR peridotites. N: number of data points; pfJ: texture index. X is parallel to the lineation and Z is normal to the foliation. The contours at multiples of a uniform distribution are plotted in an inverse log grey scale to emphasize high densities.

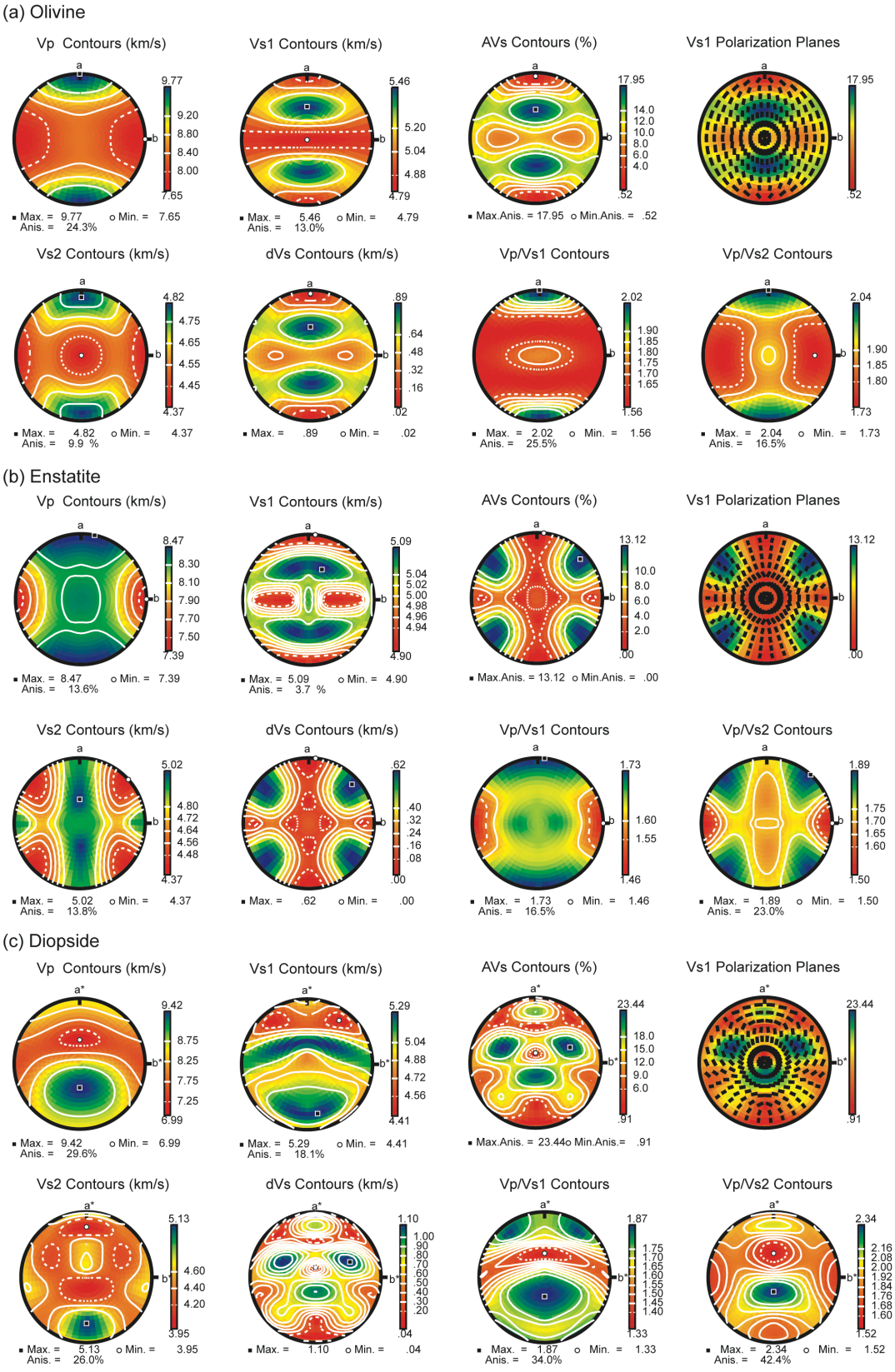

Figure S7. Equal area, lower hemisphere projection for seismic properties of olivine, enstatite and diopside. Single crystal elastic constants and density are from studies on olivine (Abramson *et al.,* 1997), enstatite (Chai *et al.,* 1997), and diopside (Collins & Brown, 1998). For diopside, the crystallographic direction of a* and b* are the poles of (100) and (010) planes, respectively.

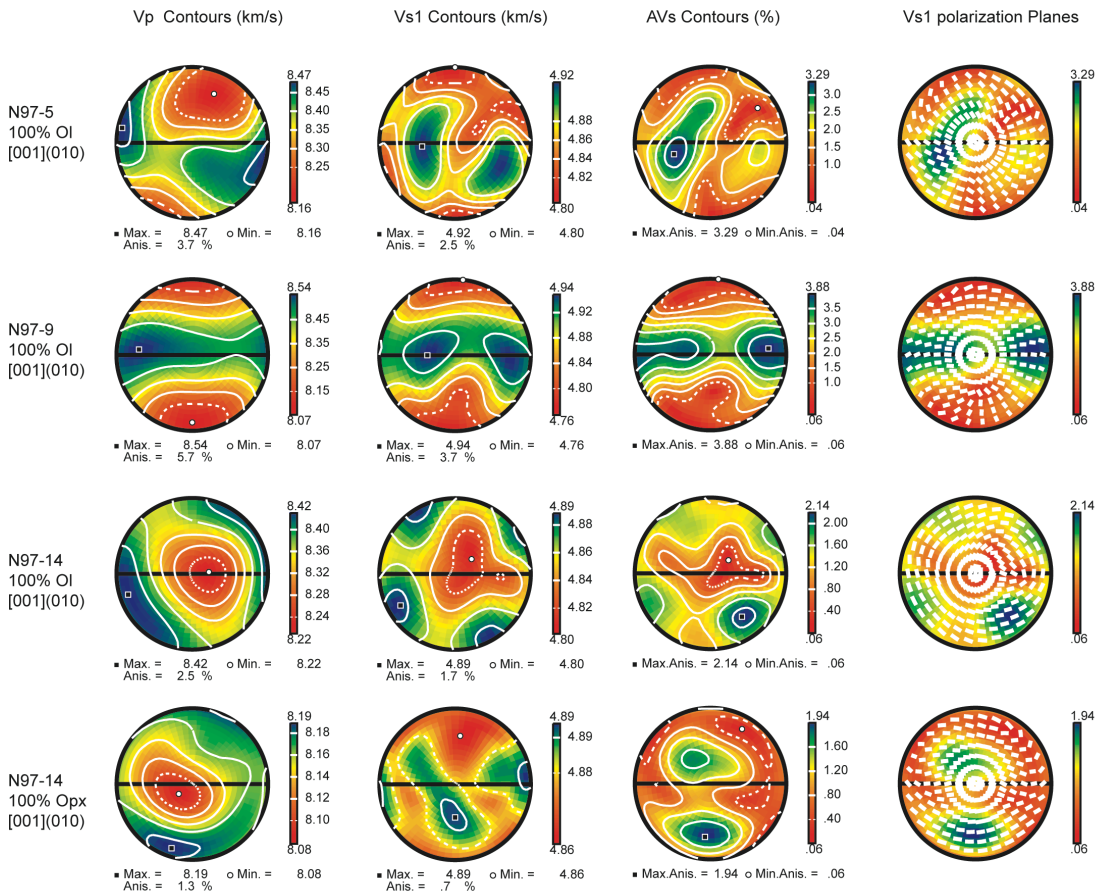

Figure S8. Calculated seismic properties of 100% olivine and 100% enstatite aggregates using the EBSD-derived CPO data for samples N97-5, N97-9 and N97-14.

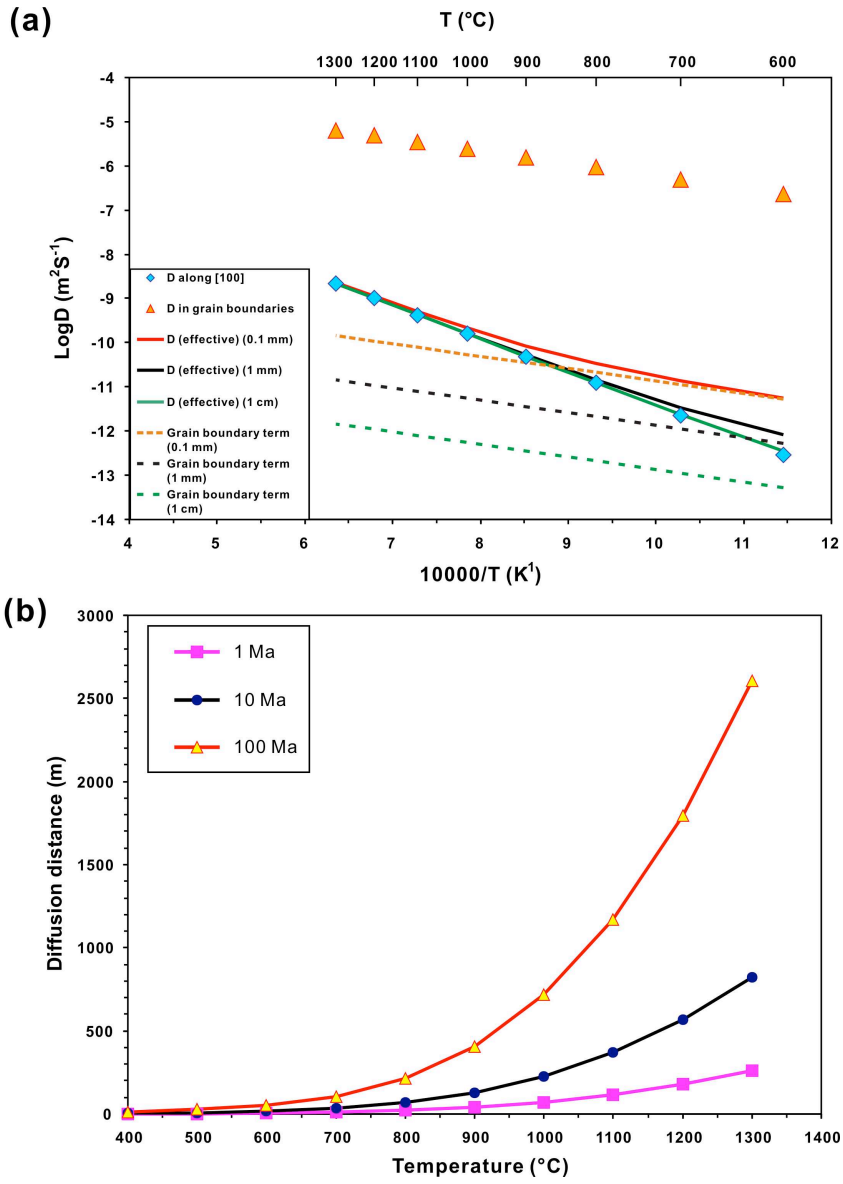

Figure S9. (a) Arrhenius diagram of various hydrogen diffusivities and (b) the effective hydrogen diffusion distance of olivine for 1 Ma, 10 Ma and 100 Ma using grain size of 1 mm. The effective hydrogen diffusion $D^{eff} = D^{[100]} + (3\delta / d)D^{gb}$, where $D^{[100]}$ is the fastest hydrogen diffusion coefficient along [100] in olivine for the "proton-polaron" mechanism and equals to $1.4\times10^{-4}\exp[-145/RT]$ (Mackwell & Kohlstedt, 1990), and D^{gb} is the hydrogen diffusion coefficient along grain boundaries and equals to $10^{-(3.4\pm0.1)}\exp[(-54\pm4)/RT]$ (Demouchy, 2010 and personal communication), d is the grain size, δ is the grain boundary width and is set to be 0.75 nm. The grain boundary term $(3\delta / d)G^{gb}$ for grain size d = 0.1 mm, 1 mm and 1 cm show ignorable effect of grain boundary diffusion on the hydrogen transport in coarse-grained peridotites.

Table S1. Whole-rock major element abundances (wt%) for peridotites from the Western Gneiss Region

Sample	N97-5	N97-14	N97-18	N97-8	N97-9	N97-13	N97-40	N97-41	GBWG	N97-30	TO	K-i-I	I-A
Lithology	garnet lherzolite	garnet lherzolite	garnet lherzolite	dunite	dunite	dunite	garnet harzburgite	garnet harzburgite	garnet wehrlite	garnet wehrlite	dunite	dunite	dunite
SiO_2	42.85	42.29	44.25	43.59	43.59	44.18	40.21	37.73	43.27	42.41	41.37	41.32	40.83
TiO_2	0.05	0.04	0.01	0.00	0.00	0.01	0.00	0.00	0.07	0.01	<0.01	0.05	0.01
Al_2O_3	1.93	2.92	2.32	0.15	0.54	0.23	1.98	1.09	2.69	1.80	0.25	0.84	0.34
Fe_2O_3	0.33	2.54	1.37	1.14	0.62	1.61	6.78	6.52	7.47	0.67	6.64	7.48	8.15
FeO	7.43	4.98	5.86	5.04	5.44	4.68				6.35			
MnO	0.13	0.14	0.13	0.09	0.11	0.11	0.11	0.09	0.08	0.11	0.08	0.10	0.10
MgO	44.67	39.01	39.69	47.63	47.19	47.6	41.23	42.99	44.03	46.73	50.81	45.74	50.04
CaO	1.46	2.49	2.10	0.04	0.07	0.11	1.17	0.54	2.35	0.60	0.06	0.62	0.03
Na_2O	0.46	0.33	0.33	0.11	0.22	0.17	0.09	0.10	0.30	0.19	<0.07	0.14	0.04
K_2O	0.02	0.01	0.01	0.02	0.01	0.01	0.00	0.00	0.00	0.01	<0.01	0.02	0.01
Cr_2O_3	0.00	0.36	0.42	0.31	0.42	0.28	0.41	0.31	0.24	0.46	0.38	0.30	0.00
NiO	0.31	0.28	0.28	0.32	0.33	0.33	0.28	0.30	0.31	0.31	0.36		
P_2O_5	0.01	0.02	0.02	0.01	0.01	0.01	0.00	0.01	0.02	0.00	<0.01	0.01	0.02
H_2O^+	0.52	3.89	2.44	0.94	1.22	0.92	7.96	10.03	0.54	0.45	0.42	4.40	
H_2O^-	0.06	0.20	0.30	0.07	0.10	0.05	0.26	0.17	0.04	0.05	0.05		0.14
CO_2	0.12	0.13	0.07	0.03	0.15	0.15	0.22	0.22	0.04	0.12	<0.01		
Sum	100.35	99.63	99.60	99.49	100.02	100.45	100.70	100.09	101.45	100.28	100.42	101.02	99.71
FeO_{tot}	7.73	7.27	7.09	6.07	6.00	6.13	6.10	5.87	6.72	6.95	5.97	6.73	7.33
Mg#	91.2	90.5	90.9	93.3	93.3	93.3	92.3	92.9	92.1	92.3	93.8	92.4	92.4

Table S2. Major element abundances (wt%) of olivine from peridotites in the Western Gneiss Region

Locality	Almklovdalen						Ugelvik, Otrøy		Gurskebotn, Gurskøy		Tafjord		
	Raudkleivane	Helgehornsvatn		Raudkleivane							Kallskaret		Kaldhusseter
Sample	N97-5	N97-14	N97-18	N97-8	N97-9	N97-13	N97-40	N97-41	GBWG	N97-30	TO	K-i-I	I-A
Lithology	garnet lherzolite	garnet lherzolite	garnet lherzolite	dunite	dunite	dunite	garnet harzburgite	garnet harzburgite	garnet wehrlite	garnet wehrlite	dunite	dunite	dunite
Analyses	13	13	16	15	17	13	6	12	12	12	12	14	15
SiO_2	40.57	41.03	41.41	40.67	41.13	41.91	40.84	41.32	41.47	41.72	41.19	41.10	40.60
TiO_2	0.01	0.02	0.00	0.01	0.00	0.00	0.02	0.01	0.01	0.01	0.02	0.02	0.02
Al_2O_3	0.00	0.01	0.00	0.00	0.01	0.00	0.01	0.01	0.01	0.01	0.01	0.01	0.01
Cr_2O_3	0.01	0.02	0.02	0.01	0.02	0.03	0.01	0.01	0.01	0.00	0.01	0.02	0.02
FeO	9.12	9.08	9.37	6.95	6.74	7.12	8.01	7.63	6.75	8.02	6.41	7.73	7.65
MnO	0.12	0.12	0.14	0.11	0.09	0.10	0.12	0.10	0.05	0.10	0.02	0.02	0.02
MgO	50.28	50.03	50.11	51.94	51.82	51.65	51.17	51.41	51.56	50.91	51.87	50.70	51.26
CaO	0.00	0.01	0.02	0.00	0.01	0.01	0.02	0.01	0.01	0.01	0.02	0.01	0.00
Na_2O	0.00	0.00	0.00	0.00	0.00	0.00	0.00	0.00	0.01	0.01	0.01	0.02	0.01
K_2O	0.00	0.01	0.00	0.01	0.01	0.01	0.01	0.01	0.01	0.01	0.01	0.01	0.01
NiO	0.43	0.40	0.42	0.44	0.41	0.01	0.41	0.40	0.32	0.44			
Total	100.54	100.73	101.51	100.14	100.24	100.83	100.62	100.91	100.20	101.23	99.56	99.63	99.59
Mg#	90.8	90.8	90.5	93.0	93.2	92.8	91.9	92.3	93.2	91.9	93.5	92.1	92.3

Table S3. Major element abundances (wt%) of orthopyroxene from peridotites in the Western Gneiss Region

Lithology	garnet lherzolite	garnet lherzolite	garnet lherzolite	dunite	dunite	garnet wehrlite	garnet harzburgite	garnet harzburgite	dunite
Sample No.	N97-5	N97-14	N97-18	N97-8	N97-13	GBWG	N97-40	N97-41	K-i-I
Analyses	15	18	10	14	16	4	11	4	3
SiO_2	57.54	58.00	58.45	57.95	59.13	58.35	57.97	58.28	56.60
TiO_2	0.03	0.03	0.03	0.01	0.00	0.07	0.01	0.01	
Al_2O_3	0.67	0.59	0.69	0.12	0.27	1.30	0.66	0.54	0.06
Cr_2O_3	0.17	0.14	0.19	0.09	0.18	0.09	0.13	0.11	0.02
FeO	6.00	5.93	5.83	4.75	4.97	4.48	5.13	4.94	5.63
MnO	0.13	0.11	0.10	0.13	0.12	0.08	0.11	0.13	0.03
MgO	35.65	35.58	35.60	36.82	36.38	36.00	36.26	36.51	36.22
CaO	0.12	0.11	0.12	0.09	0.11	0.18	0.15	0.13	0.05
Na_2O	0.00	0.01	0.00	0.01	0.00	0.00	0.01	0.01	
K_2O	0.00	0.01	0.01	0.00	0.01	0.01	0.00	0.00	0.01
NiO	0.07	0.08	0.06	0.09	0.01	0.04	0.08	0.10	
Total	100.38	100.58	101.07	100.05	101.18	100.60	100.51	100.76	98.63
Mg#	91.4	91.4	91.6	93.2	92.9	93.5	92.6	92.9	92.0
Cr#	13.9	12.7	14.8	32.4	31.6	4.9	12.6	12.2	20.7
En	91.17	91.27	91.39	93.10	92.70	93.16	92.38	92.72	91.89
Fs	8.62	8.54	8.40	6.74	7.10	6.51	7.33	7.04	8.02
Wo	0.22	0.20	0.21	0.16	0.20	0.33	0.28	0.24	0.08

Table S4. Major element abundances (wt%) of clinopyroxene from peridotites in the Western Gneiss Region

Lithology	garnet lherzolite	garnet lherzolite		garnet wehrlite		garnet wehrlite
Sample No.	N97-14	N97-18		GBWG		N97-30
Analyses	12	10	4 inclusion in grt	12	4 inclusion in grt	10
SiO_2	54.58	55.30	54.67	54.87	55.42	54.94
TiO_2	0.09	0.04	0.01	0.39	0.41	0.03
Al_2O_3	2.52	2.63	1.04	4.94	3.81	3.10
Cr_2O_3	1.26	1.47	0.73	0.99	0.93	2.62
FeO	1.96	1.62	1.37	1.06	1.33	1.45
MnO	0.03	0.03	0.06	0.04	0.06	0.03
MgO	15.47	15.60	16.93	14.50	15.47	15.43
CaO	22.02	21.93	24.28	21.94	21.31	20.55
Na_2O	1.69	1.76	0.57	2.74	2.62	1.98
K_2O	0.00	0.01	0.01	0.01	0.01	0.01
NiO	0.02	0.03	0.08	0.04	0.02	0.02
Total	99.66	100.43	99.74	101.52	101.39	100.14
Mg#	93.4	94.5	95.7	96.1	95.4	95.0
Cr#	25.3	27.3	32.3	12.2	14.0	36.7
En	47.76	48.34	48.16	46.97	49.07	49.726
Fs	3.39	2.81	2.18	1.93	2.36	2.63
Wo	48.85	48.85	49.66	51.11	48.57	47.64